Supplementary Information for "Nanotube spin defects for omnidirectional magnetic field sensing"

Xingyu Gao[†],[1] Sumukh Vaidya[†],[1] Saakshi Dikshit,[2] Peng Ju,[1] Kunhong Shen,[1] Yuanbin Jin,[1] Shixiong Zhang,[3,4] and Tongcang Li[1,2,5,6,*]

[1] *Department of Physics and Astronomy, Purdue University, West Lafayette, Indiana 47907, USA*
[2] *Elmore Family School of Electrical and Computer Engineering, Purdue University, West Lafayette, Indiana 47907, USA*
[3] *Department of Physics, Indiana University, Bloomington, Indiana 47405, USA*
[4] *Quantum Science and Engineering Center, Indiana University, Bloomington, IN 47405, USA*
[5] *Purdue Quantum Science and Engineering Institute, Purdue University, West Lafayette, Indiana 47907, USA*
[6] *Birck Nanotechnology Center, Purdue University, West Lafayette, Indiana 47907, USA*

(Dated: August 14, 2024)

I. SAMPLE PREPARATION

A. Preparation of BNNTs with spin defects

The boron nitride nanotubes (BNNTs) used in this work (sourced from Bonding Chemical and NanoIntegris) have an average diameter of about 50 nm and a typical length of 5-15 μm [1, 2]. Two typical SEM images of BNNTs are shown in Figure S1. These commercial BNNTs naturally host spin defects. The experiments shown in Figure 1-3 in the main text were performed using the as-received BNNTs without further treatment. The yield of spin defects in these BNNTs was approximately 5% according to over 100 bright emitters we have tested. To improve the probability of getting a spin defect, the BNNTs used in Figure 4-5 in the main text were treated with carbon ion implantation followed by thermal annealing for 2 hours. To create spin defects in BNNTs, we dissolve the as-received BNNT powder in ethanol and sonicated it for 10 minutes to separate the nanotubes. Then the BNNT solution is spin coated onto a Si substrate. The Si substrate with BNNTs is mounted in the home-built ion implanter and irradiated with 2.5 keV ionized CO_2 with a dose density of 10^{13} cm^{-2}. The irradiated BNNT sample is annealed at 1000 °C for 2 hours at 10^{-5} torr. About 30% of bright spots in treated BNNTs show ODMR signals. These BNNT spin defects are expected to be related to carbon atoms [3].

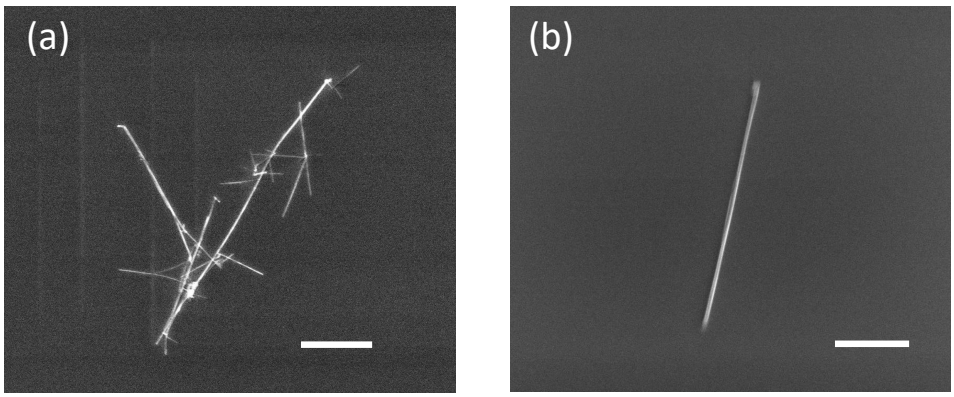

Figure S1. SEM images of (a) A cluster of BNNTs. Scale bar: 5 μm. (b) A single BNNT. Scale bar: 1 μm.

[†] These authors contributed equally to this work
[*] tcli@purdue.edu

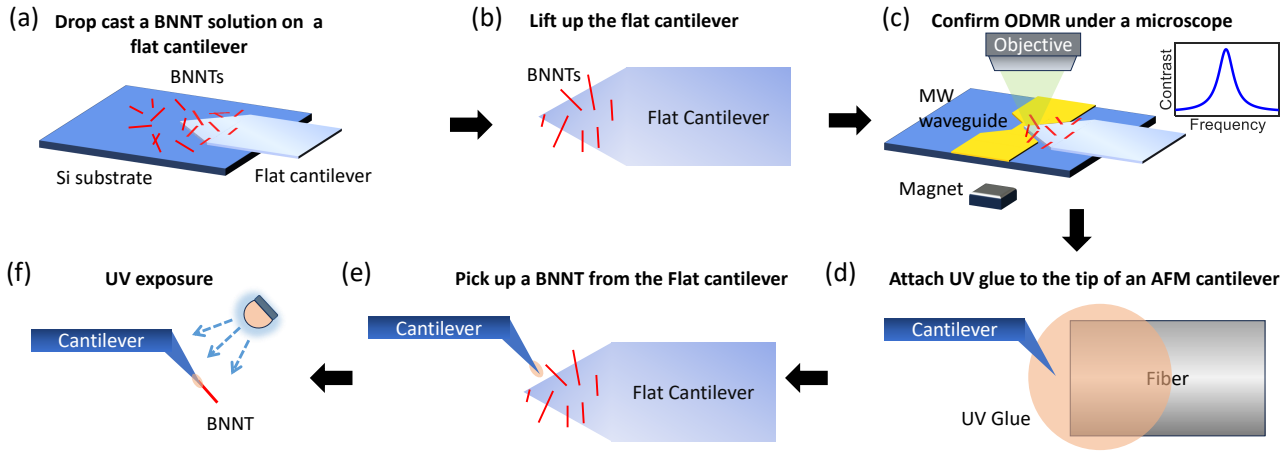

Figure S2. An illustration of the procedure to prepare a scanning probe with a BNNT containing a spin defect.

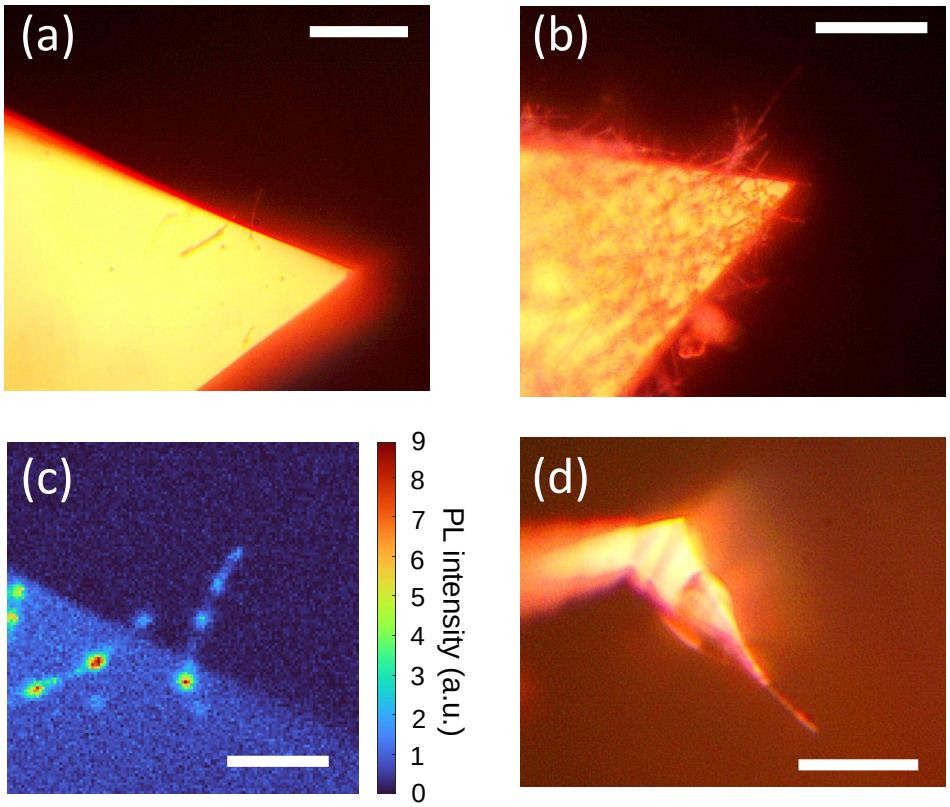

Figure S3. (a) Deposited BNNTs on a flat cantilever with one BNNT sticking out. Scale bar: 10 μm. (b) Deposited BNNTs on a flat cantilever with concentrated nanotubes. Scale bar: 10 μm. (c) A confocal image of BNNTs on a flat cantilever as shown in (a). A few isolated bright spots are observed in isolated nanotubes. Scale bar: 4 μm. (d) An optical image of a BNNT nanotube picked up by an AFM cantilever with an extended tip. Scale bar: 10 μm.

B. Transfer Boron Nitride Nanotubes to AFM cantilever tips

Figure S2 shows a general procedure to transfer a BNNT to the tip of an AFM cantilever for making a scanning probe containing a spin defect. BNNTs are first dissolved in ethanol and sonicated for 10 minutes to separate individual nanotubes. Under an optical microscope, a tipless flat silicon cantilever is brought close to a blank Si substrate from the top. After this, we drop cast BNNT solutions onto the flat cantilever, and ensure that some tubes are hanging

off the edge after solvent fully evaporates. Figure S3(a)-(b) presents two optical images after drop casting BNNTs solution on the flat cantilever. To confirm and locate the existence of spin defects, the flat cantilever with BNNTs is moved to the confocal microscope system to perform a 2D PL map as well as ODMR measurements. To deliver microwaves for testing ODMR, we use a waveguide fixed at a distance of 30μm away from the cantilever. A permanent magnet is mounted behind the sample to apply a magnetic field (typically $>$ 100 mT) to establish a large enough Zeeman splitting of BNNT spin defects.

Figure S3(c) shows a confocal image with isolated BNNTs containing bright emitters. The bright emitters were tested with ODMR experiments to confirm spin properties. After locating the BNNT with spin defects, we transfer the target BNNT to the tip of an AFM cantilever (Nanosensors ATEC-NC-10, purchased from NanoAndMore USA). A cleaved and cleaned optical fiber is used to deposit a small amount of UV epoxy onto the tip of the AFM cantilever. The AFM cantilever with UV glue on its tip is then aligned and brought close to the flat cantilever containing previously characterized spin active BNNTs. An individual BNNT is pulled out from the flat cantilever, and then the flat cantilever is removed. After this, the UV glue is exposed to a 365 nm UV lamp over 2 hours to fully cure the UV glue. An optical image of an assembled BNNT scanning probe is presented in Figure S3(d).

C. Resilience of a BNNT-AFM tip against touching a surface

Since BNNT is elastic [4], once a BNNT is attached to a AFM cantilever, it can remain stable even if it touches another surface. This is drastically different from diamond NV scanning probes. Figure S4 shows the optical images of BNNT on a AFM tip (a) before, (b) while, and (c) after touching the surface of a coverslip. We bring the BNNT on an AFM cantilever towards a coverslip and make them in contact. Remarkably, once the BNNT touches the coverslip, it bends against the surface instead of breaking or detaching from the cantilever. After moving the cantilever away from the coverslip, the BNNT remains attached to the AFM tip and retains its shape after being bent against the surface.

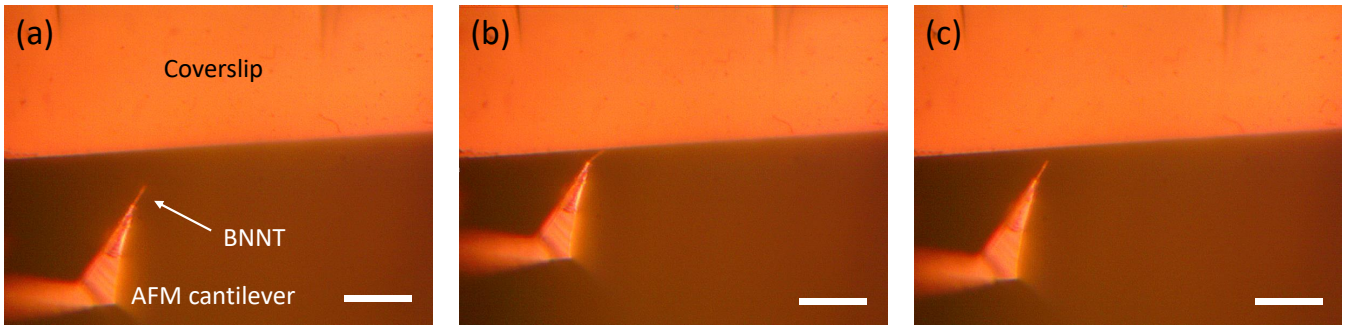

Figure S4. (a) BNNT on an AFM cantilever, before touching the surface of a coverslip. Scale bar: 10 μm (b) BNNT on an AFM cantilever, bending against the surface of a clean coverslip. Scale bar: 10 μm (c) BNNT on an AFM cantilever, after detaching from the surface. Scale bar: 10 μm

II. SPIN-1/2 GROUND STATE OF BNNT SPIN DEFECTS

To determine the ground state multiplicity of BNNT spin defects, we perform pulsed ODMR measurements to obtain their Rabi oscillation and compare their Rabi frequency with that of V_B^- spin defects taken under the same experimental conditions[5].

We assume an external magnetic field B_0 is applied along the z axis, defined by the direction perpendicular to the hBN nanosheet. Under an in-plane microwave magnetic field B_{mw} driving along the x axis with a frequency of ω_{mw}, the Hamiltonian of the ground state of spin defects (for both BNNT spin defects and hBN V_B^- defects) reads as

$$H/\hbar = DS_z^2 + \gamma_e S_z \cdot B_0 + \gamma_e B_{mw} S_x cos(\omega_{mw} t), \tag{1}$$

where S_i $(i = x, y, z)$ is the ground state spin operator, and $\gamma_e = 28.0$ GHz/T is the electron spin gyromagnetic ratio. The ZFS parameter D is 0 GHz for BNNT spin defects and is 3.45 GHz for hBN V_B^- defects. When the microwave frequency is in resonance with the spin transition frequency, the Rabi frequency is determined by the microwave field strength and the spin states. Considering the transition from $|m_s\rangle$ to $|m_s + 1\rangle$, the Rabi frequency is given as

$$\begin{aligned}\Omega_1 =& \frac{\gamma_e B_{mw}}{\hbar} \langle m_s + 1| S_x |m_s\rangle \\ =& \frac{\gamma_e B_{mw}}{2\hbar} \sqrt{S(S+1) - m_s(m_s+1)}.\end{aligned} \tag{2}$$

For S=1 ground state, this gives a Rabi frequency of $\Omega_{S=1} = \gamma_e B_{mw}/\sqrt{2}\hbar$ and, for S=1/2 ground state, the Rabi frequency is $\Omega_{S=1/2} = \gamma_e B_{mw}/2\hbar$. The multiplicities of S=1 and S=1/2 give a factor of $\sqrt{2}$ difference in Rabi frequency when the microwave field magnitude B_{mw} is fixed. For the S≥3/2 ground states, there are multiple resonances with different Rabi frequencies. Considering the S = 3/2 ground states, the transitions of $|m_s = 1/2\rangle \Leftrightarrow |m_s = 3/2\rangle$ and $|m_s = -1/2\rangle \Leftrightarrow |m_s = /2\rangle$ have Rabi frequencies of $\Omega_{S=1} = \sqrt{3}\gamma_e B_{mw}/2\hbar$ and $\Omega_{S=1} = \gamma_e B_{mw}/\hbar$, respectively. Both oscillations are faster than those of a S = 1 system. Additionally, spin defects with S ≥ 3/2 grounds state have a high formation energy, which are expected to not commonly exist in the samples.

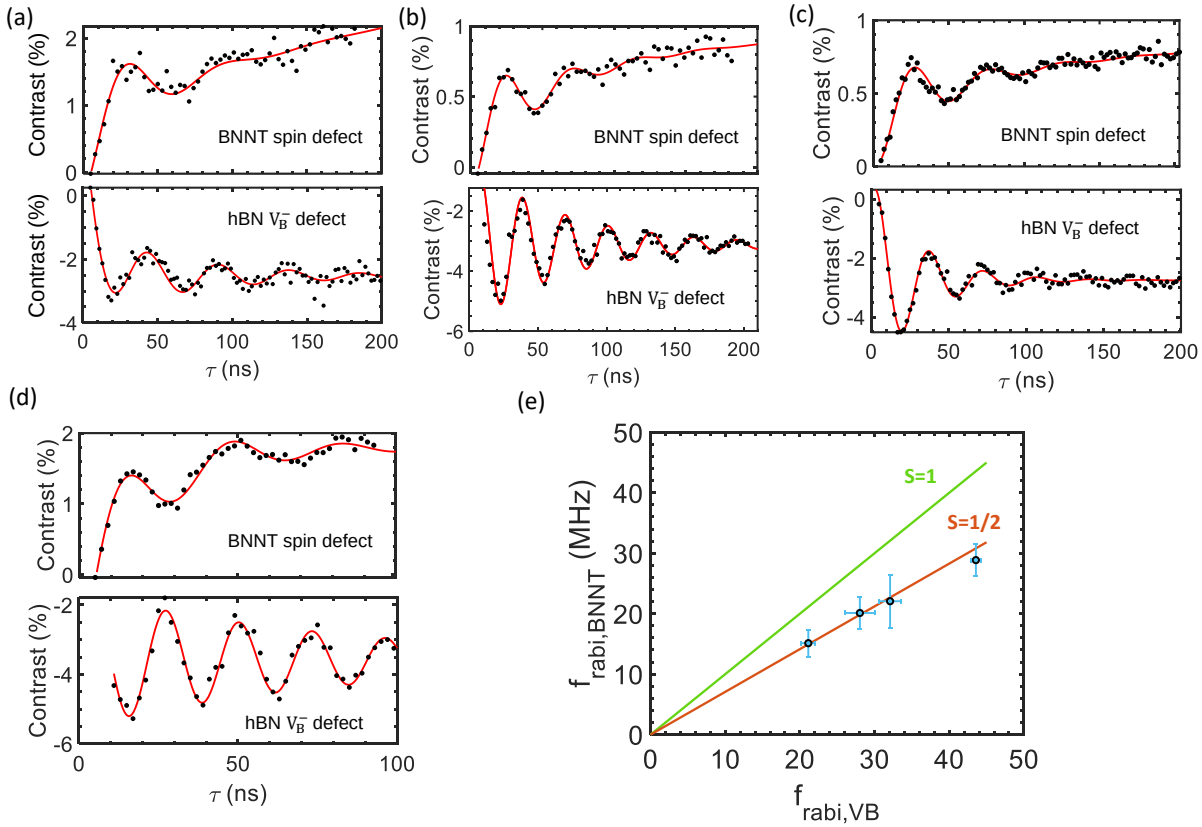

Figure S5. Confirmation of the spin-1/2 nature of the BNNT spin defects. (a),(b) Rabi oscillations of BNNT spin defects and hBN V_B^- defects, respectively. (c) Comparison of the Rabi frequency between BNNT spin defects ($S = 1/2$) and hBN V_B^- spin defects ($S = 1$).

In the experiment, we compare the Rabi frequency of BNNT spin defects with hBN V_B^- defects on same microwave waveguide and with the same input microwave power. hBN V_B^- defect is known to have S=1 ground state, so the Rabi frequency ratio between BNNT spins and V_B^- is expected to have a 1:1 dependence in case of spin-1 and a ratio of 1:$\sqrt{2}$ in case of spin-1/2. To get rid of the frequency dependent microwave transmission which affects the Rabi frequency at different driving frequencies, we tune the magnetic field to make the ODMR resonance frequency at 2.15 GHz for both BNNT spin defects and hBN V_B^-, and perform the Rabi measurement at the same microwave power. Figure S5(a)-(d)) shows examples of Rabi oscillations for the two defects taken with the same experimental parameters. A ratio close to 1:1.4 is obtained by fitting the oscillation frequencies in the two figures. By repeating the measurements at different microwave powers, the Rabi frequency of BNNT spin defects follows the theoretical prediction with the S=1/2 model (Figure S5(e)).

So far, we have assumed that only a single transition is involved in the Rabi oscillation. However, when there are multiple transitions with nearly the same resonance frequencies, the microwave will inevitably drive all these transitions together, and the Rabi frequency can differ from that obtained by driving individual transitions [6]. In our

experiments, we consider the possibility of S=1 ground states with two degenerate transitions (ZFS = 0) to explain the BNNT spin defects. Assuming that the laser initializes the spin to the $|m_s = 0\rangle$ state, the initial spin density matrix is written as

$$\rho_0 = \begin{pmatrix} 0 & 0 & 0 \\ 0 & 1 & 0 \\ 0 & 0 & 0 \end{pmatrix} \tag{3}$$

A microwave pulse with a duration time t drives both $|m_s = 0\rangle \Leftrightarrow |m_s = \pm 1\rangle$ transitions, and then the density matrix becomes

$$\rho_1 = \begin{pmatrix} \frac{1}{2}\sin^2\left(\frac{\gamma_e B_{MW} t}{\hbar}\right) & -\frac{\sqrt{2}}{4} i \sin\left(\frac{2\gamma_e B_{MW} t}{\hbar}\right) & \frac{1}{2}\sin^2\left(\frac{\gamma_e B_{MW} t}{\hbar}\right) \\ \frac{\sqrt{2}}{4} i \sin\left(\frac{2\gamma_e B_{MW} t}{\hbar}\right) & \cos^2\left(\frac{\gamma_e B_{MW} t}{\hbar}\right) & \frac{\sqrt{2}}{4} i \sin\left(\frac{2\gamma_e B_{MW} t}{\hbar}\right) \\ \frac{1}{2}\sin^2\left(\frac{\gamma_e B_{MW} t}{\hbar}\right) & -\frac{\sqrt{2}}{4} i \sin\left(\frac{2\gamma_e B_{MW} t}{\hbar}\right) & \frac{1}{2}\sin^2\left(\frac{\gamma_e B_{MW} t}{\hbar}\right) \end{pmatrix} \tag{4}$$

The resulting Rabi frequency is $\Omega_{S=1,multi} = \frac{\gamma_e B_{MW}}{\hbar}$, which is $\sqrt{2}$ times higher than $\Omega_{S=1}$ (Rabi frequency of V_B^-). This opposite to our observation, where BNNT spin defects exhibits a slower Rabi oscillation than V_B^- defects.

Here, we also note that if the S=1 spin is initialized into the $|m_s = -1\rangle$ state, the transition frequency becomes $\frac{\gamma_e B_{MW}}{2\hbar}$, the same as $\Omega_{S=1/2}$. However, at half a period, the spin state evolves into the $|m_s = +1\rangle$ state, which is experimental indistinguishable from $|m_s = -1\rangle$ when ZFS is zero. Therefore, the observed Rabi frequency from ODMR should be the same as $\Omega_{S=1,multi} = \frac{\gamma_e B_{MW}}{\hbar}$.

The above discussion assumed an ideal spin system with a single spin transition without inhomogeneous broadening. In the real experiment, all transitions have finite linewidths. Especially, hBN V_B^- defects have a relatively large linewidth. Such an inhomogeneous broadening can cause detuning and therefore affects the Rabi frequencies as

$$\Omega_1 = \sqrt{\Omega_0^2 + \delta^2} \tag{5}$$

where Ω_0 is the Rabi frequency without detuning and δ is the detuning frequency. To estimate the effect of inhomogeneous broadening, we average the Rabi oscillation over the linewidth based on the following equation[5]:

$$C(t) = C_0 \frac{\Omega_0^2}{\Omega_0^2 + \delta^2} \cos\left(\sqrt{\Omega_0^2 + \delta^2}\, t\right) \tag{6}$$

We numerically calculate the resulting Rabi oscillation for hBN V_B^- (linewidth assumed as 200 MHz) and BNNT spin defect (linewidth assumed as 80 MHz) as shown in Figure S6(a)-(b). The detuning induced by the inhomogeneous broadening increases the linewidth in the FFT spectrum by ∼10% but does not change the center frequency. The FFT of the Rabi oscillation shows a clear difference between the resonance of V_B^- and BNNT spin defects after considering the detuning caused by the inhomogeneous broadening (Figure S6(c)). This agrees with our experimental observation shown in Figure S6(d).

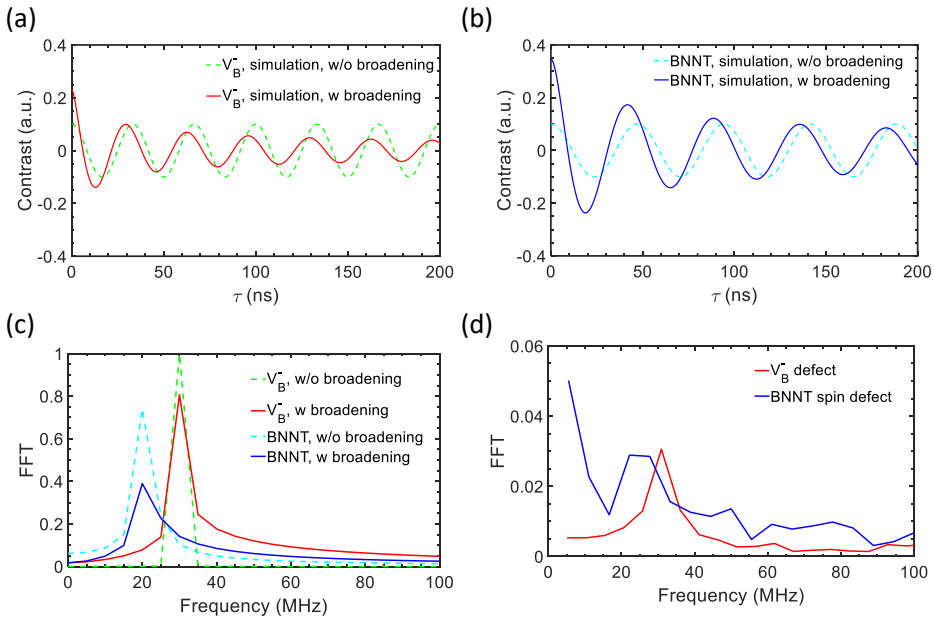

Figure S6. (a) Simulation of the V_B^- Rabi oscillation without and with the consideration of broadening. (b) Simulation of the BNNT spin defect Rabi oscillation without and with the consideration of broadening. (c) The FFT of the simulated Rabi oscillations. (d) FFT of the experimentally measured Rabi oscillations.

III. ADDITIONAL DATA FOR CHARACTERIZING SPIN DEFECTS IN BNNTS

In this section, we present the characterization results of BNNT spin defects. We first perform the pulsed measurement shown in Figure S7(a) to characterize the time dependence of the PL. A 15 μs-long laser pulse is applied every 20 ms while we record the PL counts as a function of the time when the laser is on. The 20 ms waiting time between two laser pulses makes sure that the electron fully decays back to the original state. The result shows a significant decrease of the PL brightness by ∼35% in 5 μs when the laser pulse is on. If we tune the waiting time between two laser pulses while fixing the laser duration time at 10 μs, we observe a comeback of PL brightness in the time scale of 35 μs. Here we note that such an exponential change of PL does not originate from the T_1 relaxation time of the electron spin as the decay time is much larger than the T_1 ($\sim$ 14 μs). Such a result implies that there may be a relatively long-live metastable state in the energy level structure.

Depending on different spin defects, we observe both positive and negative ODMR contrasts as shown in Figure S8(b). The magnitude of the contrast ranges from 1% to 15% among different defects. Figure S8(a) shows a possible energy level diagram of a spin-1/2 defect. The S=1/2 spin manifold is a metastable state (MS), coupled to a manifold of singlet ground and optically excited states[7, 8]. Under the green laser excitation, the electron is pumped into the excited state (ES) and then goes back to the ground state (GS) via either radiative decay with a photon emitted or spin-dependent non-radiative decay through the doublet MS. The positive and negative contrast is determined by the relatively magnitude between spin dependent non-radiative decay ratios, γ_2/γ_1 and κ_2/κ_1 (assuming both ratios are smaller than 1). If γ_2/γ_1 is larger than κ_2/κ_1, we expect to observe positive ODMR contrast. Conversely, if γ_2/γ_1 is smaller than κ_2/κ_1, we expect a negative contrast.

Now, we estimate the sensitivity of the spin defects for magnetic field sensing. For the spin defect presented in the main text (Defect 1), at 63 mT, the ODMR contrast is approximately $\sim$ 2% (Figure S9). Under a weak microwave field driving (<1 mW), the ODMR linewidth can be as narrow as 30 MHz. Since the spin defects has a spin 1/2 ground state with no zero field splitting, the quantization axis is automatically aligned to the external magnetic field. Our ODMR measurements show that the contrast of the spectrum is nearly independent of the angle of the magnetic field when the external DC magnetic field is perpendicular to the microwave magnetic field (Figure S10). Figure S10(b) shows a small decrease in the contrast when the angle is tuned larger than 30° in the xz plane. This is because the microwave field is not orthogonal to the spin defect quantization axis (the orientation of the external static magnetic field) when we tune the angle in the xz plane, and therefore the effective microwave field decreases with an increasing angle.

We now evaluate the DC and AC magnetic field sensitivity of BNNT spin defects. The DC magnetic field sensitivity

based on ODMR measurements takes the form [9]

$$\eta_{DC} \approx \frac{4}{3\sqrt{3}} \frac{h}{g\mu_B} \frac{\Delta\nu}{C\sqrt{I}}, \tag{7}$$

where $\Delta\nu$, C, I are the ODMR linewidth, ODMR contrast and PL count rate, respectively. h is the Plank's constant, $g \approx 2$ is the Landé factor, and μ_B is the Bohr magneton. Since the CW ODMR contrast and linewidth are nearly independent of the external magnetic field orientation, the sensitivity is mainly affected by the applied microwave power which affects the ODMR contrast C and the linewidth $\Delta\nu$. For a single BNNT spin defect on a gold stripline waveguide, the typical PL count rate is $\sim$ 250 kcts/s with a single-mode optical fiber (3 μm core size) to collect fluorescence light. By replacing the single-mode fiber with a graded-index multimode fiber (from Thorlabs Inc.) with a core size of 62.5 μm, the brightness is improved to $\sim$ 1.5 Mcts/s, with which we obtain the DC magnetic field sensitivity of 90 μT·Hz$^{-1/2}$.

It is noted that the sensitivities of BNNT spin defects varies among different defects. Here we list a table of the sensitivity estimated with several different defects (Table I). At different spots, the photo count rates and ODMR contrasts can differ by several times which ultimately affect the sensitivity. Nevertheless, these results display a typical value of the DC magnetic field sensitivity we obtain from the BNNT spin defects.

Defect Number#	Substrate	PL Count(kcts/s)	ODMR contrast(%)	ODMR Linewidth(MHz)	Sensitivity(μT/$\sqrt{Hz}$))
D1	gold	1500	1.4	57	91
D2	gold	500	3.3	70	80
D4	gold	900	-13.5	110	21
D6	None	200	2	80	245

Table I. Estimation of the DC magnnetic field sensivitiy based on the characterization of four spin defects. Defect 1 is presented in Figure 2-3 and Figure S9-S12. Defect 2 and Defect 4 are presented in Figure S8. Defect 6 is in the BNNT attached to a AFM cantilever used in Figure 5 in the main text. The laser power is fixed at 400 μW in all the measurements.

For AC magnetic fields, the sensitivity is given by [9]

$$\eta_{AC} = \frac{\pi}{2\gamma_e C e^{-(\tau/T_2)}\sqrt{N}} \frac{\sqrt{t_I + \tau + t_R}}{\tau}, \tag{8}$$

where C is the contrast in T_2 measurements, N is the averaged photon count in a single pulsed sequence, τ is the full field interrogation time, t_I and t_R are the initialization and readout times, respectively. In our experiment, $t_I + t_R \approx 10\ \mu s$ is required to optically polarize the BNNT spin defects. $t_I + t_R$ is much larger than T_2. Therefore, in this limit, the AC magnetic field sensitivity is proportional to T_2: $\eta_{AC} \propto T_2$. Taking Defect 1 as the example, by applying pulsed ODMR, we characterize the spin coherence properties at 63 mT. The spin relaxation time of BNNT spin defects is found to be $T_1 = 14\ \mu$s and the spin coherence time in a Hahn echo pulse sequence is $T_2 = 109$ ns (Figure S12). Using the measured contrast $\sim$ 1.5% and averaged count per sequence, $N \sim 3$, the AC magnetic field sensitivity is given as 170 μT·Hz$^{-1/2}$, which is close to the DC magnetic field sensitivity.

A. Pulsed PL measurements

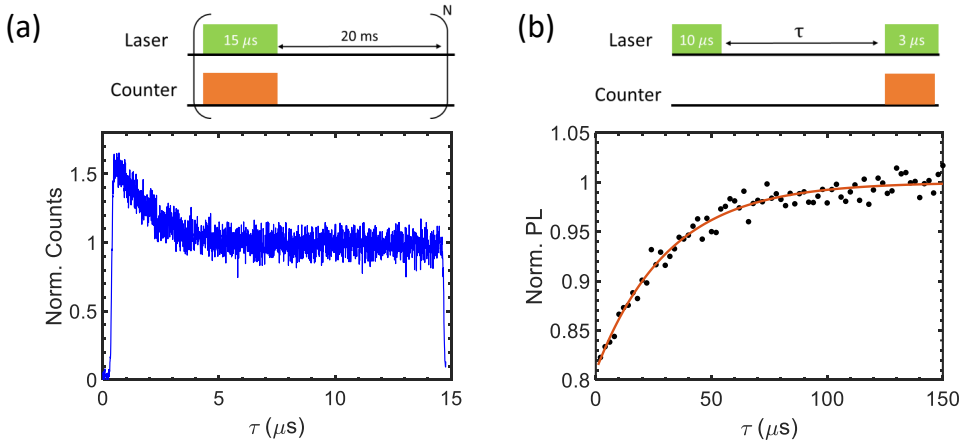

Figure S7. (a) PL counts as a function of time during the laser pulse. (b) PL counts as a function of delay time.

B. Electronic energy structure

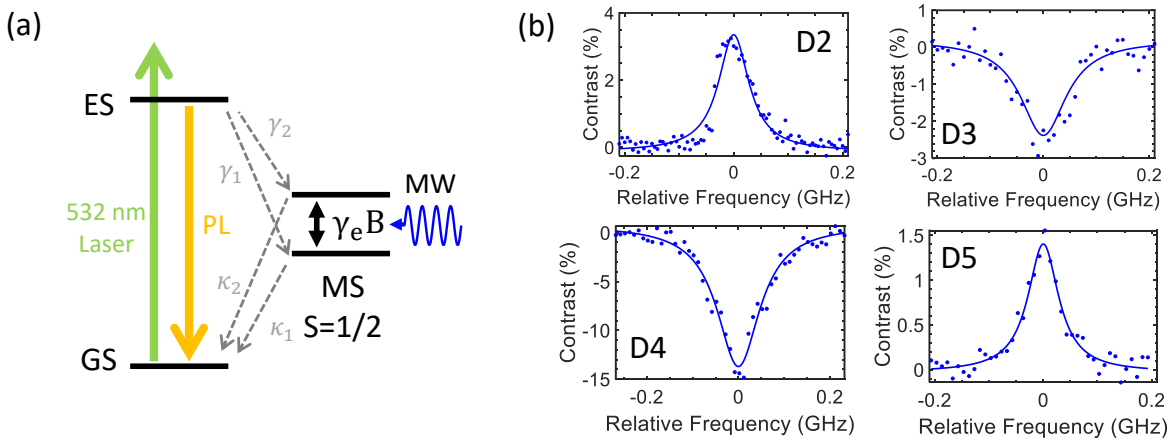

Figure S8. (a) A possible energy level diagram depicting the electron spin dynamics under laser and microwave excitation[7, 8]. The spin defect contains a singlet ground state (GS), a singlet optically excited state (ES) and a doublet metastable state (MS). The greens arrow is the spin conservative excitation under 532 nm laser pumping. The orange arrow is spontaneous emission from ES to GS. Gray dashed lines are non-radiative decays. An external magnetic field can cause a splitting of $\gamma_e B$ in the MS via the Zeeman effect. A microwave (MW) is applied to drive the electron spin in MS. (b) Typical ODMR spectra of different BNNT spin defects placed on a gold stripline.

C. Power dependence of the ODMR spectrum

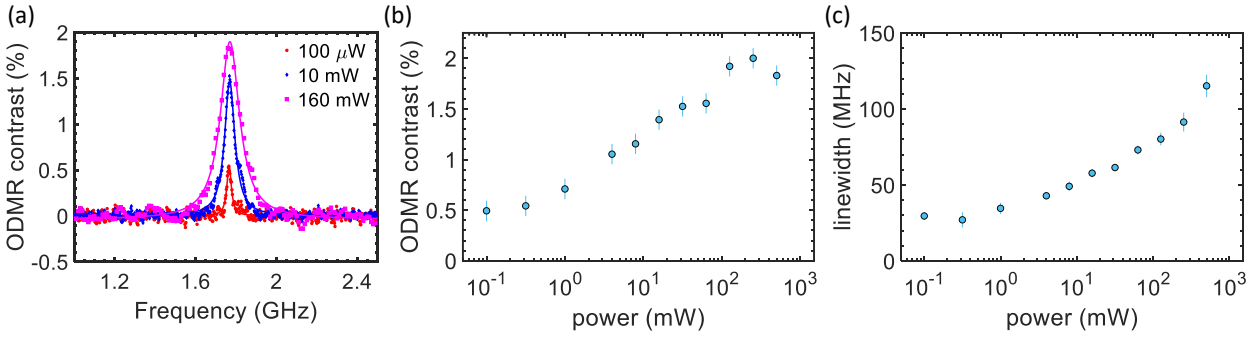

Figure S9. (a) Three examples of CW ODMR spectra taken at different microwave powers. (b) ODMR contrast as a function of the microwave power. (c) The linewidth of the ODMR resonance as a function of the microwave power.

D. Angle-dependent ODMR measurements

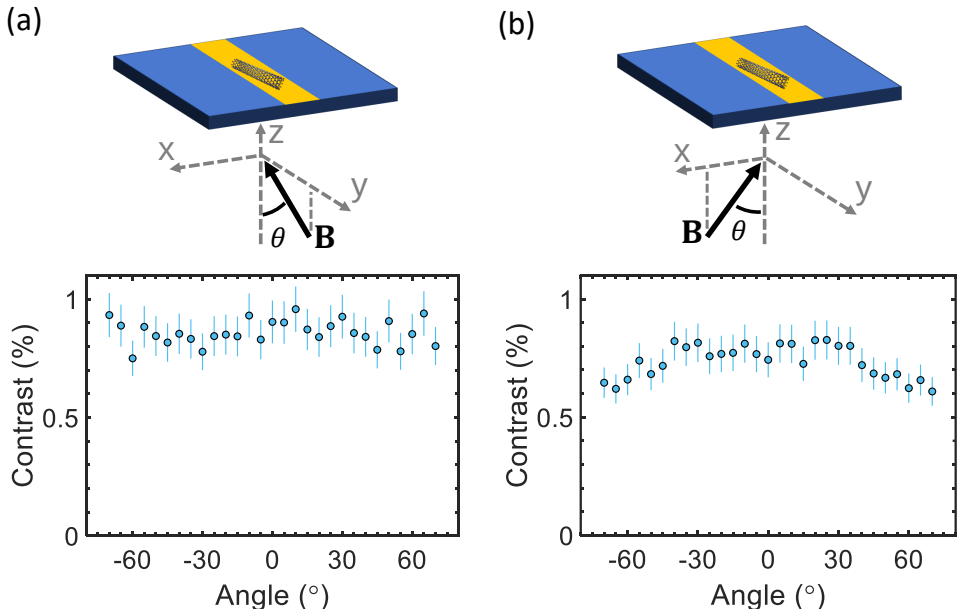

Figure S10. (a) ODMR contrast as a function of the angle θ for a magnetic field in the $y-z$ plane. (b) ODMR contrast as a function of the angle θ for a magnetic field in the $x-z$ plane.

E. DC magnetic field sensitivity

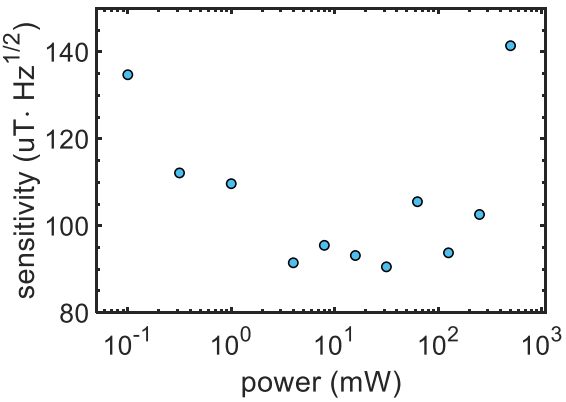

Figure S11. DC magnetic field sensitivity of a single BNNT spin defect as a function of microwave power. It is calculated based on the dependence of the ODMR contrast and linewidth on the microwave power shown in FigureS9. The photon count rate is 1.5 Mcts/s by using a graded-index multimode fiber at 400 μW laser excitation.

F. Coherence properties of spin defects in BNNT

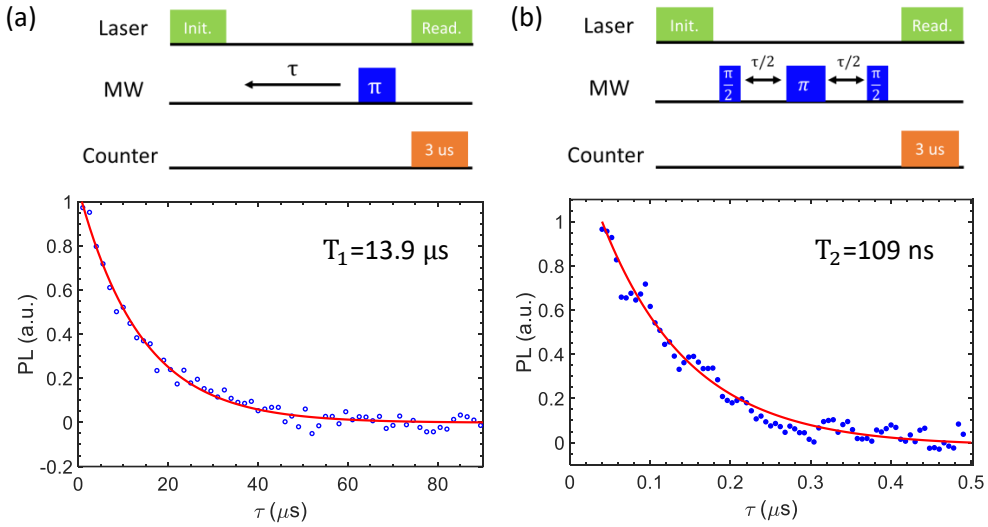

Figure S12. (a) T_1 measurement shows a typical relaxation time of 14 μs. (b) T_2 measurement shows a typical coherence time of 109 ns.

IV. MEASUREMENTS OF THE STRAY MAGNETIC FIELD GENERATED BY A Fe_3GeTe_2 FLAKE

In Figure 4 of the main text, we used spin defects in BNNTs as a local sensor to measure the local stray magnetic field from a Fe_3GeTe_2 (FGT) flake. The FGT flake was exfoliated from a large crystal and transferred onto a gold waveguide on a sapphire substrate. Then we deposited carbon-doped BNNTs on top of both the gold stripline and the FGT flake. Spin defects on the gold served as a reference for results on the FGT flake. In Figure S13(a), an optical image shows a cluster of BNNTs on both the FGT and the gold stripline. An external magnetic field of ~19.4 mT is applied in in-plane or out-of-plane. The magnetic field will induce Zeeman splitting of BNNT spin defects. Since the

BNNT spin defects have a negligible ZFS, equal magnitudes of both in-plane and out-of-plane magnetic fields yield identical energy splits for spin states without the FGT flake's influence. The electron spin resonance (ESR) frequency is given by $f_0 = \gamma B_{ext}$, where $\gamma = 28.0$ GHz/T is the gyromagnetic ratio of the BNNT spin defect. In the presence of proximate FGT flake, the local stray field can induce additional Zeeman splitting, which can be measured by the frequency shift in the ESR spectrum. Similarly, the total magnetic field is obtained by the ESR resonance frequency as $f_1 = \gamma B_{tot}$. Therefore, the local stray magnetic field B_s can be extracted from the difference of the resonance frequencies

$$B_s = B_{tot} - B_{ext} = \frac{f_1 - f_0}{\gamma}. \tag{9}$$

When the magnitude of the external magnetic field, B_{ext}, greatly exceeds the stray magnetic field from the sample, B_s, the BNNT spin defect predominantly senses the component of the stray magnetic field aligned with B_{ext}, denoted as $B_{s,\parallel}$. This is due to the approximation $\sqrt{(B_{ext} + B_{s,\parallel})^2 + B_{s,\perp}^2} - B_{ext} \approx B_{s,\parallel}$ being valid when $|B_{ext} + B_{s,\parallel}|$ is much larger than $|B_{s,\perp}|$. Here, $|B_{s,\perp}|$ represents the stray magnetic field component perpendicular to B_{ext}. By varying the direction of B_{ext}, we can probe the stray magnetic field in various orientations.

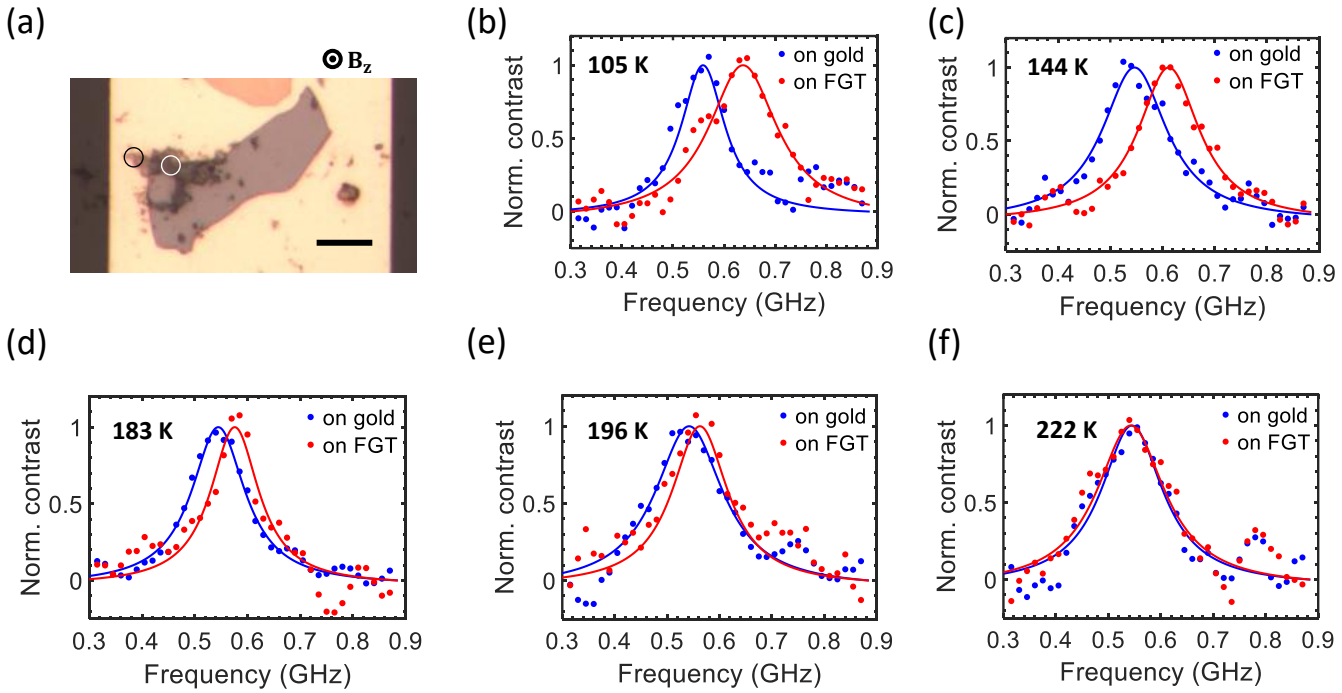

Figure S13. Sensing the stray magnetic field of FGT using BNNT spin defects. (a) An optical image of BNNTs containing spin defects deposited on a FGT flake (white circle) and on the gold waveguide(black circle). The scale bar is 10 μm. (b-f) Measured ODMR spectra of the BNNT spin defects on the FGT flake (red) and on the gold surface (blue) when the temperature is 105 K (b), 144 K (c), 183 K (d), 196 K (e), and 222 K (f). Note that the Curie temperature of FGT is about 220 K. The external magnetic field is applied out-of-plane with a magnitude of 19.4 mT.

We measure the ESR spectra of BNNT spin defects at various temperatures ranging from 90-300K to characterise the stray magnetic field at the location of the defect. With an out-of-plane external magnetic field, as we cool down the sample, an increase in the ESR frequency shift is observed when the system is below the FGT's Curie temperature (∼220 K). With an in-plane magnetic field approximately along the long axis of the FGT flake, no discernible ESR frequency shift is observed within the temperature range of our the experiment. This shows the FGT flake is anisotropic and has an out-of-plane easy axis as expected.

Since FGT has anisotropic magnetic properties with an easy axis along the out-of-plane direction, when the sample is cooled down below T_c in a small in-plane field, the spins in the FGT flakes are expected to be slightly canted away from the out-of-plane direction and there is a small net magnetization. On the other hand, since the up-spin and down-spin states are degenerate when the field is in-plane, there will be multiple domains, with some of them having a net moment pointing up and the others pointing down. The overall net magnetization in the out-of-plane direction

can be zero or small enough beyond the detection limit. This also explains that no discernible ODMR frequency shift is observed in our experiment for the in-plane case.

By depositing BNNT's onto the magnetic sample, the positions of the BNNT spin defects are not precisely controlled since they are randomly distributed among the nanotubes. This limits its functionality for studying the stray field across the sample surface. By attaching a BNNT with a characterized spin defect to a scanning probe AFM tip, one can map the stray magnetic field in 2D or even 3D with an improved spatial resolution.

V. SCANNING PROBE MEASUREMENTS OF STRAY MAGNETIC FIELD

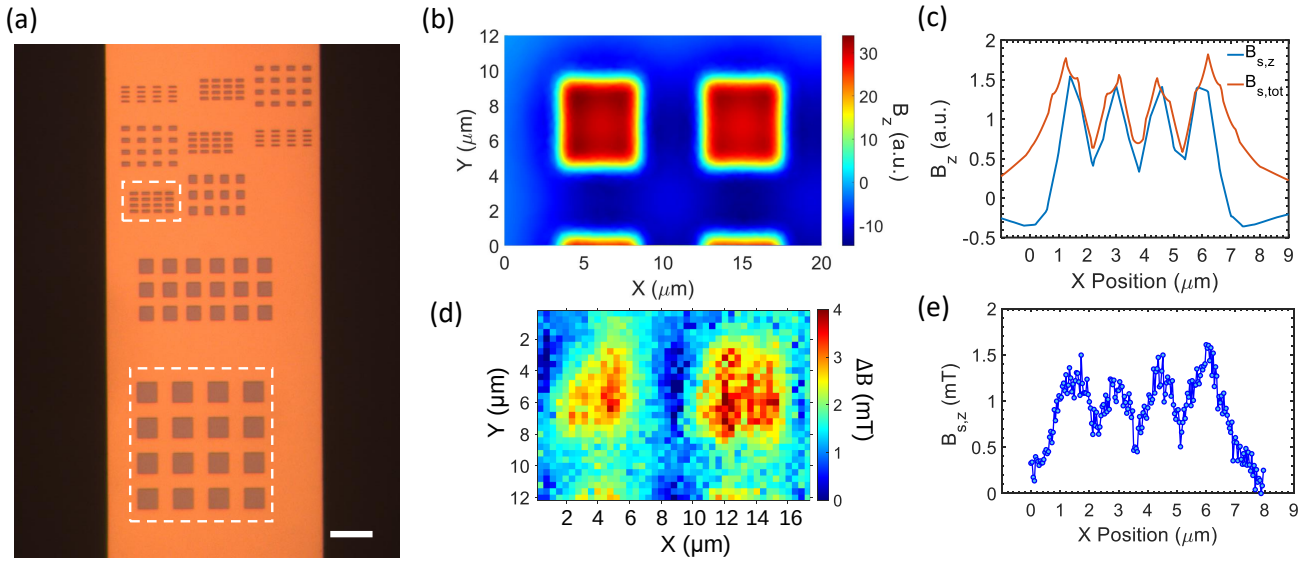

Figure S14. (a) An optical image of the gold microwave waveguide with nickel patterns. The dashed boxes highlight the patterns that we characterize with scanning probe magnetometry. The scale bar is 10 μm. (b)-(c) Simulation results of the stray magnetic field distributions from nickel patterns of (b) 5 μm $\times$ 5 μm for each patch and (c) 600 nm $\times$ 2 μm for each patch. The experimental results correspond to these simulations are shown in (d) and (e) respectively.

In Figure 5 of the main text, we use scanning probe ODMR measurements to image the local stray field near the nickel pattern. In the scanning probe measurements, the tip of the BNNT probe is first brought to a distance of $\sim$10 μm using the knobs on the translation stage manually. Then the tip is further brought close to the surface via a piezo positioner. During the scanning probe magnetometry, the distance between the sample and tip of BNNT is maintained the same at hundreds of nanometer. The minimum distance we can achieve is limited by the precision and stability of our piezo positioner. Further improvement of the sample-sensor distance can be realized by implementing a closed-loop pizeo positioner to enable a more reliable feedback control.

We simulated the expected stray field distribution for a 700 nm distance from the Nickel pattern (Figure S14). The experimental results show good qualitative agreements with the simulated results of the stray field along the axis of external magnetic field. As discussed in the previous section, the strong external magnetic field ($\sim$95 mT) greatly suppresses the Zeeman effect from the transverse component (perpendicular to the external field) of the stray field. More precise information about the probe-to-sample separation is required for a precise quantitative comparison.

[1] Jonghoon Ahn, Zhujing Xu, Jaehoon Bang, Andres E Llacsahuanga Allcca, Yong P Chen, and Tongcang Li. Stable emission and fast optical modulation of quantum emitters in boron nitride nanotubes. *Optics letters*, 43:3778–3781, 2018.

[2] Ryan Starko-Bowes, Xueji Wang, Zhujing Xu, Sandipan Pramanik, Na Lu, Tongcang Li, and Zubin Jacob. High-temperature polaritons in ceramic nanotube antennas. *Nano Letters*, 19(12):8565–8571, 2019.

[3] Noah Mendelson, Dipankar Chugh, Jeffrey R Reimers, Tin S Cheng, Andreas Gottscholl, Hu Long, Christopher J Mellor, Alex Zettl, Vladimir Dyakonov, Peter H Beton, et al. Identifying carbon as the source of visible single-photon emission from hexagonal boron nitride. *Nature materials*, 20:321–328, 2021.

[4] Dmitri Golberg, Pedro MFJ Costa, Masanori Mitome, and Yoshio Bando. Properties and engineering of individual inorganic nanotubes in a transmission electron microscope. *Journal of Materials Chemistry*, 19(7):909–920, 2009.

[5] Sam C Scholten, Priya Singh, Alexander J Healey, Islay O Robertson, Galya Haim, Cheng Tan, David A Broadway, Lan Wang, Hiroshi Abe, Takeshi Ohshima, et al. Multi-species optically addressable spin defects in a van der waals material. *arXiv preprint arXiv:2306.16600*, 2023.

[6] Malcolm H Levitt. *Spin dynamics: basics of nuclear magnetic resonance*. John Wiley & Sons, 2013.

[8] Raj N. Patel, Rebecca E. K. Fishman, Tzu-Yung Huang, Jordan A. Gusdorff, David A. Fehr, David A. Hopper, S. Alex Breitweiser, Benjamin Porat, Michael E. Flatté, and Lee C. Bassett. Room temperature dynamics of an optically addressable single spin in hexagonal boron nitride. *Nano Letters*, 24:7623–7628, 2024.

[7] Islay O Robertson, Benjamin Whitefield, Sam C Scholten, Priya Singh, Alexander J Healey, Philipp Reineck, Mehran Kianinia, David A Broadway, Igor Aharonovich, and Jean-Philippe Tetienne. A universal mechanism for optically addressable solid-state spin pairs. *arXiv preprint arXiv:2407.13148*, 2024.

[9] A. Dréau, M. Lesik, L. Rondin, P. Spinicelli, O. Arcizet, J.-F. Roch, and V. Jacques. Avoiding power broadening in optically detected magnetic resonance of single nv defects for enhanced dc magnetic field sensitivity. *Phys. Rev. B*, 84:195204, Nov 2011. doi:10.1103/PhysRevB.84.195204. URL `https://link.aps.org/doi/10.1103/PhysRevB.84.195204`.